Journal of Colloid and Interface Science 626 (2022) 1015–1027

Contents lists available at ScienceDirect

Journal of Colloid and Interface Science

journal homepage: www.elsevier.com/locate/jcis

Micellar entanglement and its relation to the elastic behavior of wormlike micelle fluids

Ricky F. López-Santiago [a], Jorge Delgado [b], Rolando Castillo [a,*]

[a] Instituto de Física, Universidad Nacional Autónoma de México, P.O. Box 20-364, 01000 Mexico City, Mexico
[b] División de Ciencias e Ingenierías, Campus León, Universidad de Guanajuato, León, Guanajuato, Mexico

GRAPHICAL ABSTRACT

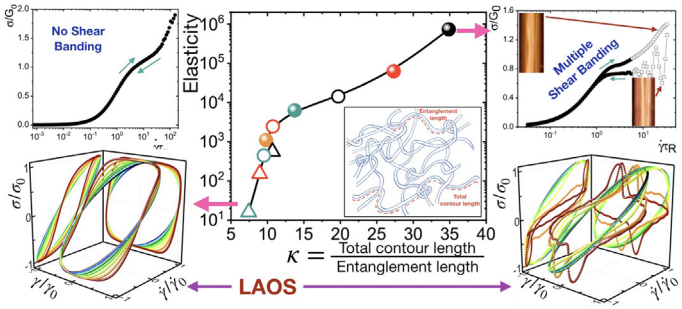

ARTICLE INFO

Article history:
Received 4 May 2022
Revised 29 June 2022
Accepted 1 July 2022
Available online 05 July 2022

Keywords:
Wormlike micelles
Rheology
Micro-rheology
LAOS
Viscoelastic spectra
Elastic forces

ABSTRACT

Hypothesis: The elastic contribution to the fluid dynamics of wormlike micellar solutions makes these fluids unique due to the distinctive self-assembled micellar network formed by tubular micelles. Measured mesoscopic scales of the micellar network related to the degree of entanglement can give guidelines for understanding the origin of elastic forces and their effect on rheological response.
Experiments: Different experiments were made as flow curves, rotating the internal or external cylinder in a Couette geometry, small and large oscillatory shear tests, and linear shear banding observations, all of them to determine how elastic forces modify the rheological behavior in systems made of different ratios of hexadecyltrimethylammonium bromide (CTAB)/sodium salicylate (NaSal) and different ratios of CTAB/$NaNO_3$. Diffusive wave spectroscopy micro-rheology was also performed to measure the mean square displacements of microspheres embedded in the micellar fluids to obtain their high-frequency viscoelastic spectra. With this information, the entanglement index κ, the ratio of the total contour of the micelles to the entanglement length, was estimated and correlated with the rheological behavior.
Findings: The entanglement index is a valuable piece of information to understand the origin of the contribution of the elastic forces from a molecular point of view on the fluid dynamics of wormlike micelle solutions.

1. Introduction

A large number of solutions embedded with large semiflexible cylindrical aggregates (Wormlike Micelles, WLMs) present a shear stress that relaxes approximately as in the Maxwell model, $G(t) = Go \exp(-t/\tau_R)$ at long times, or equivalent, at low and interme-

* Corresponding author.
E-mail address: rolandoc@fisica.unam.mx (R. Castillo).

https://doi.org/10.1016/j.jcis.2022.07.003
0021-9797/

diate frequencies, ω, in its related complex modulus $G^*(\omega) = i\omega\tilde{G}(\omega) = [G'(\omega) + i\,G''(\omega)]$; [1] several exceptions to that rule are well known [2,3]. The elastic modulus, G_o, and the relaxation time, τ_R, can be obtained from the linear viscoelastic spectrum from the crossing between the $G'(\omega)$ and $G''(\omega)$ curves [4]. According to the reptation-reaction model, an average chain length dominates relaxation if the micellar breaking and reformation processes are faster than their reptation. Here, simple mono-exponential stress relaxation is ensued, with a relaxation time equal to the geometric mean of two characteristic times: The time for micellar breaking and recombination, and the time for micellar reptation.

When WLM fluids are submitted to a steady flow, they can show a transition between a homogeneous and nonhomogeneous flow state where macroscopic bands coexist along the gradient direction [5,6]. They arise at a not entirely flat plateau in the shear stress (σ) versus shear rate ($\dot{\gamma}$) flow curve [7]. Shear banding is a consequence of a mechanical instability, where the multivalued nonmonotonic constitutive curve presents $d\sigma/d\dot{\gamma} < 0$, producing two branches, separated by a plateau, one at low and another at high shear rates. The mechanical stability requires fluid separation; although shear stress is almost constant throughout the solution, but the bands show different shear rates [5-7]. In many cases, band volumes follow approximately an expression equivalent to the lever rule [5]. Shear banding is similar to a nonequilibrium phase coexistence between an isotropic and a strongly aligned phase (paranematic), which has a lower viscosity than the quiescent phase [5,8-10].

In a shear banding simple scenario, the fluid is just divided into two macroscopic regions separated by a thin steady interface of finite width [11,12]. At high shear rates, the paranematic phase shows a strong birefringence related to micellar orientational order, where neutron scattering has confirmed a nematic signature of this phase [11,12]. The other region is made mainly of isotropic fluid that flows at a low shear rate. The kinetics of banding-structure formation and the spatiotemporal dynamics of the interface between bands in the shear banding flow have been studied, revealing the existence of a destabilization process that is not well understood [13]. The picture of two stable shear bands separated by a steady interface presents theoretical challenges [14,15]. Studies of linear stability of the shear banded planar Couette flow using the Johnson-Segalman model fluid, for the case of no stress diffusion, show that flow is unstable for almost all arrangements of the two gradient shear bands for long waves [14]. For the case of weak diffusion, a small stabilizing effect is present, although the basic long-wave instability mechanism is not affected.

Viscoelastic properties of WLM solutions of CTAB (hexadecyltrimethylammonium bromide) in water with different proportions of NaSal (sodium salicylate) have been studied for a long time [16-20]. When increasing the shear rate, gradient shear banding is observed, even without increasing the ionic force of the media [21]. The larger the imposed shear rate at the plateau, the larger the amount of highly birefringent fluid. When shear banding is achieved, velocity profiles have confirmed the existence of two bands with different shear rates in the semidilute regime (CTAB/NaSal: *100/50 mM*) [22,23]. Delgado *et al.* [24] compared the rheological behavior of two micellar solutions of CTAB/NaSal with $R = 2$ and $R = 4$ (R = [NaSal]/[CTAB], [CTAB] = *100 mM*) in the semidilute regime under Couette flow moving the internal cylinder of the geometry; the external cylinder is static. The authors obtained velocity profiles employing a two-incident beam laser Doppler technique, revealing that one of the micellar solutions ($R = 2$) becomes heterogeneous a long time after flow inception, even at very low imposed shear rates. These profiles do not correspond to what is expected for gradient shear banding. At low shear rates, $\dot{\gamma} < 0.45\ s^{-1}$, the fluid splits in one section close to the moving cylinder, where the local mean velocity depends linearly on the gap position, and in a second section with significant velocity fluctuations. The fluid essentially does not flow in a third section close to the static cylinder; it behaves like a slipping block. The picture of two stable shear bands separated by a thin steady interface does not occur. Inhomogeneous flow could be observed, although it cannot be classified as a simple scenario of shear banding. However, the former slipping block flows at high imposed shear rates and presents a linear profile. At $\dot{\gamma} > 0.45\ s^{-1}$, velocity profiles are consistent with gradient shear banding. On the contrary, for $R = 4$, the flow never became heterogeneous even at high shear rates. Another system that has been thoroughly studied is CTAB/$NaNO_3$, which presents shear banding depending on the $NaNO_3$ concentration at a constant temperature [25], and their bands follow a simple scenario in some circumstances, although it can present secondary flows [26].

The viscoelastic spectrum given by Small-Amplitude Oscillatory Shear (SAOS) has been extensively studied to quantify micellar systems' viscoelastic properties. However, interesting nonlinear effects occur if the strain amplitude is increased using a Large-Amplitude Oscillatory Shear (LAOS) [27]. Since the stress response of viscoelastic materials is typically independent of the shear direction, the shear stress waveform contains only odd higher harmonic contributions. In the time-dependent strain-imposed oscillatory protocol, the fluid sample is subject for times $t > 0$ to a strain of the form $\gamma(t) = \gamma_o sin\ \ \omega t$, which corresponds to a strain rate $\dot{\gamma}(t) = (\gamma_o\omega)\cos\omega t = \dot{\gamma}_o\cos\omega t$. After an initial transient (many executed cycles), the system's response is expected to attain a state that is time-translationally invariant from cycle to cycle. An appealing feature of LAOS in Maxwellian fluids is that the harshness of the flow's time dependence, relative to the fluid's intrinsic relaxation timescale, τ_R, can be tuned by varying ω in the applied oscillation without sudden jumps in the strain input, as in step experiments [28]. LAOS experiments can explore the full range between steady-state and strongly time-dependent behaviors by investigating the effect of two characteristic dynamic variables, the Deborah number, *De*, and the Weissenberg number, *Wi*. The former, $De = \tau_R/T$, is defined as the ratio of a characteristic relaxation time of a material τ_R and a characteristic time scale of observation of the deformation process, T, which is the inverse of angular frequency $T = 1/\omega$, in oscillatory flow. The latter, $Wi = \tau_R/T_d$, characterizes the ratio of elastic to viscous forces, *i. e.*, the ratio of τ_R and a characteristic time of the deformation process T_d. For steady shear, T_d is the inverse of the instantaneous shear rate $T_d = 1/\dot{\gamma}$, whereas for oscillatory shear, $T_d = 1/\dot{\gamma}_o = 1/(\omega\,\gamma_o)$ [27]. It is generally expected to have a linear response when the applied strain remains very small $\gamma_o << 1$, or when the ratio of elastic to viscous forces is small, corresponding to Wi << 1. In the same way, when the ratio of a characteristic relaxation time and the time scale of observation of the deformation process is small, De << 1, we expect a reconfiguration dynamics that keep pace with the applied deformation. This will lead to a quasi-steady state response in which the stress slowly sweeps up and down the steady-state flow curve as the shear rate varies through a cycle. In contrast, for De $\gg$ 1, the system's relaxation dynamics cannot keep pace with the applied deformation, and we expect an elastic-like response. In addition, in LAOS, shear banding has been experimentally observed [29]. Some models have been capable of predicting shear banding in LAOS protocol, as those using the partially extending convected (PEC) equation [30] or the VCM model (Vasquez–Cook–McKinley) [31]. However, to study shear banding theoretically in different experimental protocols, the model must include nonhomogeneous flow, and a criterion for the onset of shear banding. It is not enough to consider that the underlying constitutive curve of stress as a function of strain rate is nonmonotonic

[32]. The formation of shear bands in LAOS has been successfully studied using the Rolie-Poly (RP) model for polymers and WLM solutions [33]. Here, the authors adopted a single-mode approach, taking into account just one reptation relaxation timescale and one stretch relaxation timescale. Shear banding also appears when the constitutive curve is monotonic. Chain breakage and recombination narrow the relaxation spectrum significantly such that the single-mode approach adopted provides a complete picture of the parameter space. Here, shear banding is significant, and the mechanisms that trigger its onset were identified, focusing on the physical understanding of the shapes of the curves of stress versus strain or strain rate.

In simple fluids in steady shear flow (Newtonian fluids), flow tends to become unstable and eventually turbulent because of inertia when the Reynolds number, $Re = \tau_1\dot{\gamma}$, significantly increases. Here, $\dot{\gamma}$ is a characteristic deformation rate, and $\tau_1 = \rho d^2/\eta$ is a characteristic time of the fluid, the viscous diffusion time, where d is a characteristic length in the velocity gradient direction, η is the viscosity, and ρ is the mass density. In Taylor-Couette (TC) flow, Taylor showed that the purely azimuthal base flow becomes unstable when the Taylor number $Ta_i = \Lambda^{1/2}Re$ exceeds some critical value, $Ta_{ic} \sim 41$, if only the inner cylinder of radius R_i rotates with a small gap, d, between the cylinders. Here, $\Lambda = d/R_i$ <<1 denotes the dimensionless curvature of the streamlines. In contrast, in non-Newtonian fluids, as in WLM fluids, the stress relaxation brings up an additional time scale τ_R. Here, another route to instabilities exists, which does not involve inertia and is referred to as purely elastic. If Re << 1, the *Wi* number takes the role of the control parameter that can lead to the emergence of secondary flows and eventually to elastic turbulence [26]. Homogeneous flow becomes unstable when $Ta_e = \Lambda^{1/2}Wi$ exceeds some critical value Ta_{ec}. However, it is important to mention that the appropriate dimensionless group for a purely elastic instability only comes from the high shear rate band [26]. If both *Re* and *Wi* are large, flow instabilities are referred to as inertio-elastic. In this case, a precise instability scaling is lacking even for the TC geometry. It has been suggested [25], by dimensional analysis, that the Taylor number should be written as $Ta = \Lambda^{1/2}f(Re, Wi)$ where f goes to *Re* when $EI \rightarrow 0$, and f goes to *Wi* when $EI \rightarrow \infty$, where $EI = Wi/Re = \tau_R/\tau_1$ is the elasticity number, which is the ratio of elastic forces to inertial forces within a fluid [30,34].

Re and *Wi* numbers are rates between different forces involved in the flow dynamics of a fluid. However, from a different perspective, they are not measuring directly any intrinsic property related to the micelle network, which is responsible for the elastic forces in the fluid when it is deformed during the flow. In the semidilute region, micro-rheology using Diffusing Wave Spectroscopy (DWS) has provided estimations for the relevant scales of the micellar network, such as micellar total contour lengths, persistent lengths, entanglement lengths, and mesh sizes [35-38]. If the flow process is very slow, one could expect that the micellar network slowly disentangles, contributing to some extent to the elastic forces involved in the flow. However, if the micellar network is deformed fast, not allowing enough time for the tubular micelles to disentangle due to the speed of the imposed strain, the network's contribution to the elastic forces involved in the flow would increase. One quantity that somehow measures the relative entanglement of a micellar network would be the ratio of the total contour length of the micelles in the network to their entanglement length, which, as mentioned, can now be experimentally estimated.

This paper aims to assess some rheological features, considering the role of elastic forces in the flow dynamics in typical micellar solutions that self-assemble in WLMs for understanding their rheological behavior better. To this end, we need WLM solutions where relaxation times can be tuned through concentration or temperature changes to exhibit a wide range of behaviors that can be described by shear flow curves, viscoelastic spectrum, and shear banding patterns. Mixtures of CTAB with different salts give an excellent choice to fulfill these requirements, such as CTAB/NaSal and CTAB/$NaNO_3$. Some of the questions to be addressed here are: If elastic forces are significant, When are the thixotropic flow curves reliable? Moreover, Does gradient shear banding follow a simple scenario or a multiple banded one?; Is some underlying reason that explains the different behavior of micellar solutions of CTAB/NaSal with $R = 2$ and at $R = 4$, at different temperatures, and those of CTAB/$NaNO_3$, which presents shear banding depending on the CTAB concentration at a constant temperature?; In a WLM solution, Is there a way to relate the mesoscopic length scales of the micellar network related to the degree of entanglement to the solutions' elasticity number?

2. Experimental

2.1. Materials

Hexadecyltrimethylammonium bromide (CetylTrimethylAmmonium Bromide, CTAB, purity > *99%*, Sigma-Aldrich), sodium salicylate (NaSal, purity *99.5%*, Sigma-Aldrich), sodium nitrate ($NaNO_3$, purity > *99%*, Sigma-Aldrich). Reagents were used as received. All samples were prepared with ultrapure deionized water (Nanopure, USA).

2.2. Rheological measurements and observation of shear banding

Rheological measurements were performed with a MCR-702 TwinDrive rheometer (Anton Paar, Austria), in which two air-bearing supported electrically commuted motors are sitting opposite each other. Both motors are controlled by the same digital signal processor controller, allowing different testing modes. In the separate-motor-transducer mode, both motors are employed, although in a synchronized way. One motor is kept at a fixed position and managed only as a torque transducer, while the other motor exclusively functions as a drive unit.

An instrument with a transparent Couette cell geometry was developed in our lab to observe the gradient shear banding in micellar solutions with two concentric quartz cylinders (50 mm height). The external cylinder (*I. D. 80 mm/O. D. 85 mm*) rotates thanks to an electrically controlled motor, and the inner cylinder (*I. D 70 mm/O. D. 75 mm*) is fixed and filled with water coming from a thermal regulated circulatory bath for thermal control; a similar design was presented previously in Ref. [39]. The gap between cylinders is 2.5 mm wide. The fluid in the gap is visualized with the aid of a CCD camera (Hamamatsu Vidicon, Japan) and a zoom lens focused on a sheet of light in the gradient-vorticity plane made with a Ne–He laser beam (Coherent Inc., USA) and a combination of spherical and cylindrical lenses.

2.3. Mesoscopic scales of the micellar network obtained by DWS micro-rheology

The micellar network mesoscopic scales of interest in WLM solutions that can determine their rheological behavior are the micelles' total contour length, L_C, both persistence, l_p, and entanglement, l_e, lengths, as well as the mesh size of the entangled micellar network, ξ. Our group has developed a procedure for measuring these mesoscopic scales by measuring the mean square displacement of tracers dispersed in the WLM solution, using a quasi-elastic multiple light scattering method (Diffusive Wave Spectroscopy, DWS), described in a review paper [38]. In this method, negatively charged polystyrene microspheres (*Diam. = 784 nm*;

Bangs Labs, USA), used as tracers, are dispersed in the WLM solutions. The Mean Square Displacement (*MSD*) of these embedded particles is measured with DWS and related to viscoelastic spectrum $G^*(\omega)$, from low to high frequencies, using a generalized Stokes-Einstein equation [38,40]. In this way, DWS microrheology reaches a bandwidth far beyond the conventional mechanical rheometry, allowing us to observe more features in the spectra. From $G^*(\omega)$, using approximate relations coming from theory, the mesoscopic scales in the WLM solutions can be evaluated. Our DWS setup is a homemade instrument described in Ref. [38]. It is important to note that several small but significant changes have been made to the original formulas developed to estimate these characteristic lengths over the last decade. They were incorporated into the formulas just to be mentioned.

The physical concepts for evaluating these scales are summarized here: At time scales shorter than WLM breakage time corresponding to high frequencies, the Maxwellian stress relaxation processes are fundamentally frozen; WLMs behave like semiflexible polymer chains. Then, stress relaxes, first dominated by the Rouse-Zimm modes and at higher frequencies by internal relaxation of Kuhn segments. $G^*(\omega)$ exhibits, at those frequencies, a power-law behavior, $|G^*| \sim \omega^{\nu}$, with the exponent $\nu \sim 5/9$ in the Rouse-Zimm regime, which shifts to $\nu \sim 3/4$, where the internal bending modes of Kuhn segments dominate. That change occurs at a frequency ω_o ($\omega_o \approx k_BT/8\eta_s l_p^3$; η_s is the solvent viscosity) [41] that corresponds to the shortest relaxation time in the Rouse-Zimm spectrum. From ω_o coming from the slope change in $|G^*(\omega)|$, l_p can be obtained, and the other characteristic lengths can be evaluated. The WLM network mesh size can be obtained in the loose entanglement regime with $\xi \cong (A\ k_BT/G_o)^{1/3}$, where the prefactor A = 9.75 is a recent correction [31]. In the same way, l_e can be calculated using $l_e = \xi^{5/3}/l_p^{2/3}$ [42]. From $G''_{min}/G_o \cong (l_e/L_C)^{0.8}$, the total contour length can be estimated by incorporating breathing and high-frequency Rouse modes. The exponent in this equation is a correction given by Granek [43]. Here, G''_{min} is a local minimum of $G''(\omega)$ after the first crossing between $G'(\omega)$ and $G''(\omega)$. In summary, once G_o, G''_{min}, and ω_o are experimentally obtained, the characteristic lengths (l_e, l_p, ξ, and L_C) can be calculated.

3. Results and discussion

3.1. SAOS and flow Curves

Viscoelastic spectra using SAOS of micellar solutions were made at low and intermediate frequencies, and the corresponding G_o and τ_R parameters were determined (Fig. SM2). For CTAB/NaSal solutions with *R = 2* and at *R = 4,* ([CTAB] = *0.1 M*), measurements were made at different temperatures (*20 – 40 °C*), and for CTAB/$NaNO_3$ solutions at different surfactant concentrations at *30 °C* ([CTAB] from *0.1* to *0.3 M*, and [$NaNO_3$] = *0.3 M*). Although the elastic modulus does not change significantly for CTAB/NaSal solutions, it is not the case for τ_R, which is quite different in both systems at temperatures below *30 °C*; above this temperature, the difference in τ_R is not significant, as observed in Fig. 1. The inset of Fig. 1 presents τ_R for the different micelle solutions of CTAB/$NaNO_3$; in this case, G_o increases with surfactant concentration. Temperature or surfactant concentration controls the rheological response through τ_R and G_o.

As we will see, the relaxation time differences will make the micellar solutions of CTAB/NaSal with *R = 2* and *R = 4* behave quite differently below 40 °C. In particular, at *R = 2,* this solution presents gradient shear banding; this is not the case for *R = 4* [24]. CTAB/$NaNO_3$ solutions present linear shear banding at concentrations above *0.1 M* in CTAB.[25].

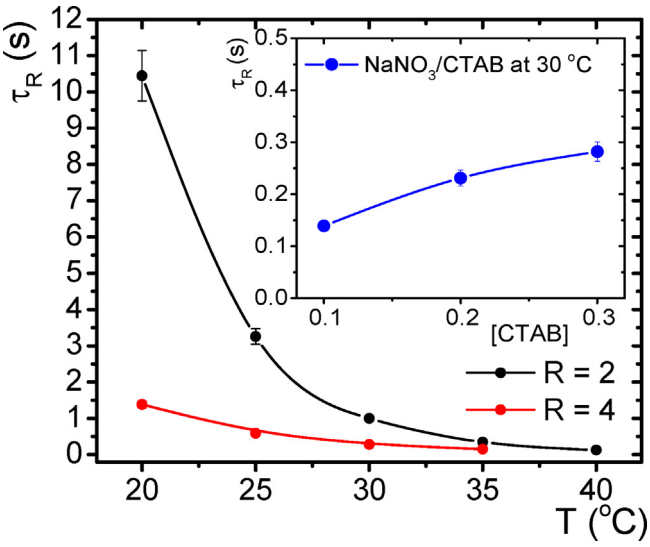

Fig. 1. τ_R *vs.* temperature for micellar solutions of CTAB/NaSal with *R* = 2 and *R* = 4 ([CTAB] = *0.1 M*). Insert, τ_R *vs.* CTAB concentration micelle solutions of CTAB/$NaNO_3$, ([$NaNO_3$] = *0.3 M*) at 30 °C. All data were determined from SAOS viscoelastic spectra. In some cases, error bars are smaller than the symbols in the figures.

For the case of CTAB/NaSal with *R = 2* and at *R = 4*, we developed shear flow curves following a protocol for observing the consequences of rheometric measurements performed faster than τ_R. In logarithmic mode, our rheometer spends a time $t^{measuring}$ executing a measurement depending on the shear rate, according to the formula $t^{measuring} = b \cdot \dot{\gamma}^m$, where *b* and *m* are constants determined by the experimenter, first selecting the number of required points to be measured in a whole shear flow experiment, and then selecting the shear rate and the time spent for the first measurement, as well as, for the last one; details in Fig. SM1. We define $t^{rel} = t^{measuring}/\tau_R$, which determines how long the measurement time is relative to the relaxation time; it is like the inverse of the Deborah number. In addition, we can rotate the internal or external cylinder of the Couette geometry. We expect that they will give the same result. Fig. 2 presents scaled flow curves, σ/G_o *vs.* $\dot{\gamma}\tau_R$, for thixotropic loops where the shear rate is first ramped up (up-shear curve) to some maximum value, then ramped down (down-shear curve) at different temperatures, *T = 20*, *25*, and *30 °C*. Measurements were made, rotating the external or the internal cylinder while maintaining the other cylinder static. In these flow curves, the time used to measure each point of the flow curve is different. When the symbols are open at $t^{rel} < 1$, the measurements fluctuate significantly, and the flow curves present hysteresis. When the symbols are filled $t^{rel} > 1$, both fluctuations and hysteresis are pretty low. We present the average of two or more measurements in the mentioned figures. Flow curves are essentially the same when $t^{rel} > 1$, no matter what cylinder is moved, but when $t^{rel} < 1$, flow curves do not coincide. As temperature increases, τ_R is pretty small; therefore, it is not feasible to make rheological measurements with the $t^{rel} < 1$ condition, as it occurs at 35 °C (not shown). Here, all curves behave the same way as in the long-time measurements. As a corollary, thixotropic loops with low fluctuations and small hysteresis are obtained when times larger than τ_R are used during each measured point. The up-shear and down-shear curves coincide no matter what cylinder is rotating.

Fig. 3 presents scaled flow curves (σ/G_o *vs.* $\dot{\gamma}\ \tau_R$) for up-shear and down-shear curves for CTAB/NaSal with *R = 4*, and in the inset for CTAB/$NaNO_3$; in all the cases, $t^{rel} > 1$. The curves present neither fluctuation nor hysteresis, and the up- and down-shear curves are almost identical; they do not depend on the rotating cylinder.

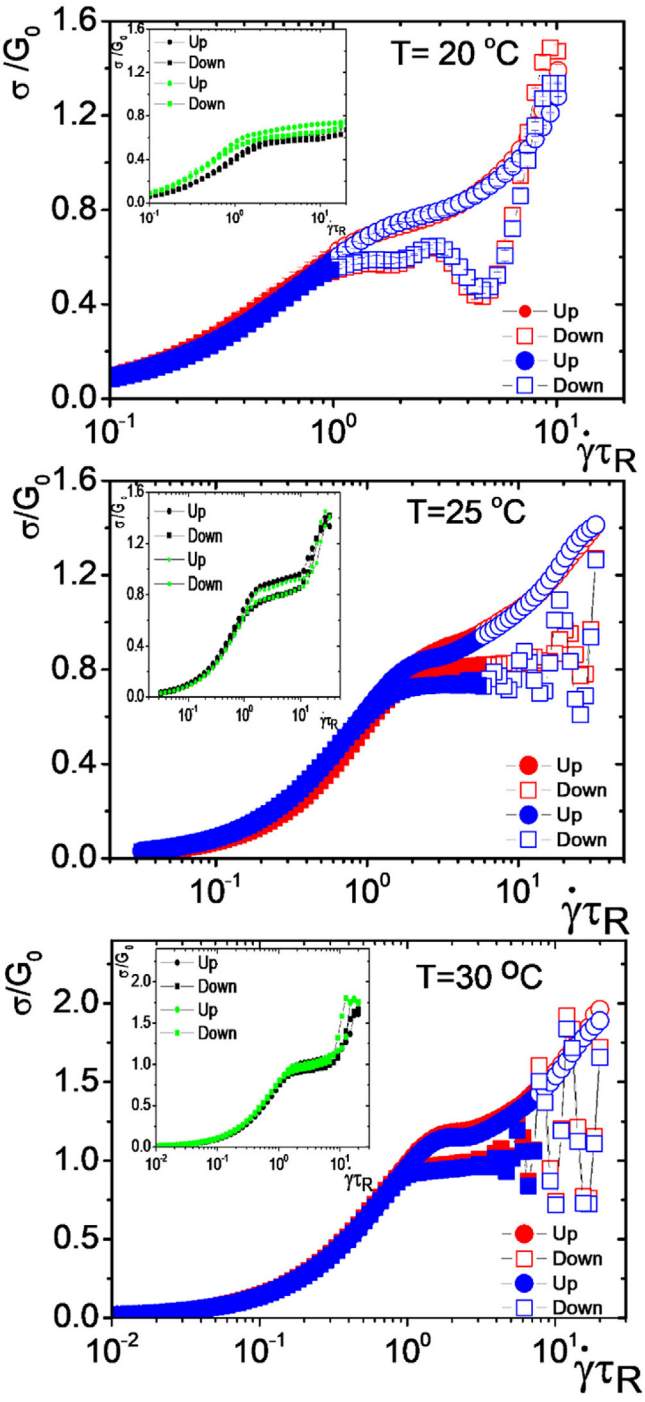

Fig. 2. Flow curves for the CTAB/NaSal micellar solutions with $R = 2$ made in Couette geometry at different temperatures where the inner or external cylinders rotate while the other cylinder remains static. Up-shear curves (Up) are circles, and down-shear (Down) curves are squares: inner rotating cylinder red symbols, external rotating cylinder blue symbols. The time used to measure each point of the flow curve is different: Full symbols correspond to measurements where $t^{rel} > 1$. On the contrary, empty symbols correspond to $t^{rel} < 1$. Insets: Same measurements as in the main figure. Up-shear curves (Up) are circles, and down-shear (Down) curves are squares. Inner rotating cylinder black symbols, external rotating cylinder green symbols; for all the cases $t^{rel} \geqslant 10$.

The same occurs for CTAB/NaSal with $R = 4$ as the temperature is varied. Equivalent flow curves to those presented before for $t^{rel} < 1$, as mentioned above, are not feasible to obtain for these solutions because the relaxation times are pretty low, as in the case of

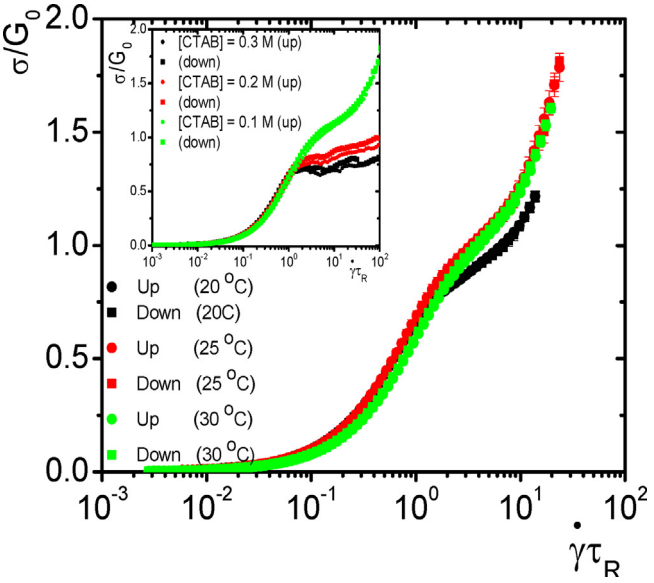

Fig. 3. Flow curves for the micellar solutions performed at $t_{rel} > 1$: CTAB/NaSal ([CTAB] = *0.1*), $R = 4$ Inset: CTAB/NaNO3 at 30 °C. All of them are made in a Couette cell geometry. Up-shear curves (Up) are circles, and down-shear (Down) curves are squares. In all curves, the internal cylinder is the rotating one.

CTAB/NaSal with $R = 4$ where τ_R = *1.4*, *0.59*, and *0.28 s* for *20*, *25*, and *30* °C, respectively.

In summary, determining if a thixotropic loop is reliable or not depends on the value t_{rel} for each point of the flow curve. For $t^{rel} > 1$, the system has enough time to relax, *i. e.*, micelles have enough time to disentangle. Nevertheless, when $t^{rel} < 1$, there is not enough time for the tubular micelles to disentangle due to the speed of the imposed strain, and the micellar network is deformed, so the contribution of elastic forces increases modifying the flow curves. The more entangled the micellar network, the more significant time for micellar disentanglement. We will go back to this issue below. However, we can observe another feature in this case, when the ratio of elastic to viscous forces is small, *i. e.*, Wi < 1, we do not observe differences in the flow curves for all the cases of the implemented protocol. For Wi > 1, the elastic contribution to the dynamic forces during the flow produces different flow curves, as observed in Fig. 2.

3.2. Large amplitude oscillatory strain

LAOS strain-imposed protocol was performed on the WLM solutions under study, which follow the Maxwell model at low and intermediate frequencies when the applied strain is small $\gamma_o << 1$ (SAOS). The stress, $\sigma(t)$, in the Maxwell model for an oscillatory shearing strain of amplitude $\gamma_o = Wi_o/De$ and angular frequency $\omega = De/\tau_R$, can be written as $\sigma(t) = (Wi_o/De)[G'\sin(De/\tau_R)t + G''\cos(De/\tau_R)t]$, where $G' = G_o[De^2/(1 + De^2)]$ and $G'' = G_o[De/(1 + De^2)]$. The loci of $\sigma(t)$ *vs.* $\gamma(t)$ for this model is an ellipsis given by $\sigma^2 - 2G'\sigma\gamma + (G'^2 + G''^2)\gamma^2 = [G'' Wi_o/De]^2$, where the stress maximum in a general linear viscoelastic material always occurs in the first quadrant (all variables positive) of a σ *vs.* γ graph ($\sigma^{max} = \gamma[(G'^2 + G''^2)/G']$). The response of WLM solutions to oscillatory shearing strain is probed by selecting γ_o, which in LAOS is not limited to small values, producing deviations from the linear behavior (Maxwell model). For a fixed Wi_o value, when $De \gg 1$, WLM solutions can display a nonlinear elastic response at frequencies whose periods are shorter than the time scale needed to form shear bands, particularly when $Wi_o/De > 1$. In general, when the ratio of relaxation time to the time scale of the deformation observation (*De*

<< *1)* is quite small, a reconfiguration dynamics that keeps pace with the applied deformation is expected. This flow leads to a quasi-steady state response, in which the stress slowly sweeps up and down as the shear rate varies through a cycle. Time-resolved small-angle neutron scattering *t*-SANS in a WLM solution,[29] similar to those studied here, have identified different frequency regimes matching nearly perfectly the expectations of the linear viscoelastic Maxwell model.

Selected results are illustrated in Figs. 4 - 6 using Pipkin diagrams for scaled 3D Lissajous-Bowditch curves (σ/σ_o *vs.* γ/γ_o and $\dot{\gamma}/(\gamma_o\ \omega)$) and their projections (elastic representation: σ/σ_o *vs.* γ/γ_o or viscous representation: σ/σ_o *vs.* $\dot{\gamma}/(\gamma_o\ \omega)$) (original experimental data in Fig SM3). In these diagrams, we vary De ($=\tau_R\omega$) and Wi_o ($=\tau_R\omega\gamma_o$ = *De* γ_o). Here, σ_o is the maximum shear stress in an oscillation cycle used for scaling the shear stress. The flow does not necessarily remain homogeneous, as observed in other WLM systems depending on the involved Wi_o and *De* numbers. [29] In the mentioned figures, rows are arranged for different *De* ($=\tau_R\omega$) values, *i. e.* varying the frequency of shear oscillation; then, in a row, we present on the left results for $De \sim 0.3$, in the center for $De \sim 1$, and on the right for $De \sim 3$. τ_R is varied due to shifting the surfactant concentration (Fig. 4) or temperature (Figs. 5 and 6). Top rows correspond to large τ_R values, which decrease downward. The 3D Lissajous-Bowditch curves and their projections are more or less similar for each system going down along a specific column because graphs are in scaled variables; we will go back to this issue below. In contrast, more significant behavior changes are observed in all the systems going from left to right along a row. Moving rightward along a row in these figures, the system's relaxation dynamics cannot keep pace with the applied deformation. In these

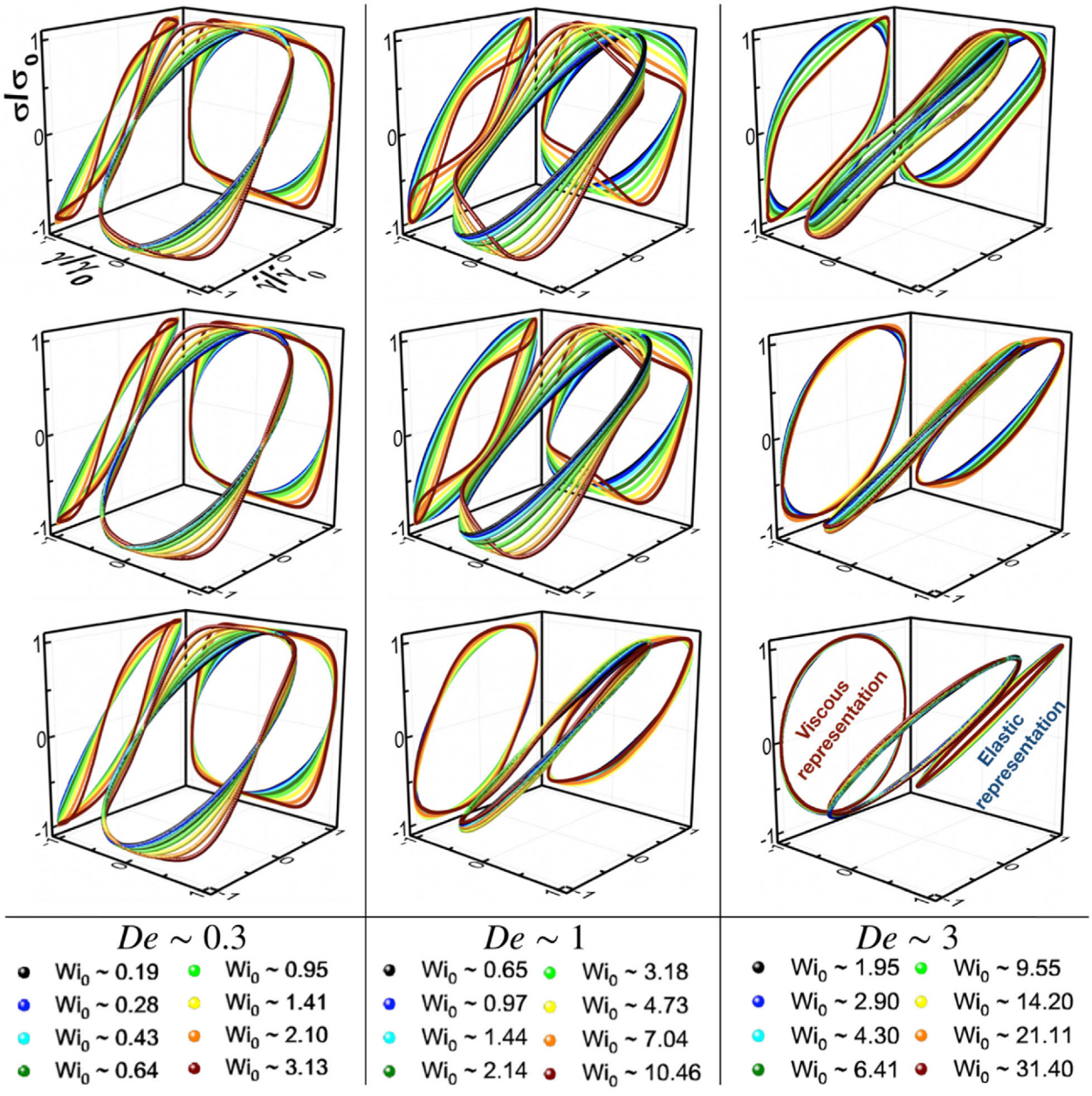

Fig. 4. Normalized 3D Lissajous-Bowditch curves and their projections (elastic representation: σ/σ_o *vs.* γ/γ_o or viscous representation: σ/σ_o *vs.* $\dot{\gamma}/(\gamma_o\ \omega)$) for CTAB/$NaNO_3$ micellar solutions at different Wi_o ($=\tau_R\omega\ \gamma_o$) and *De* ($=\tau_R\omega$). Surfactant concentration from the upper row to the lower one: [CTAB] = *0.3, 0.2,* and 0.1 M, respectively; *[*$NaNO_3$*] = 0.3 M*, and *T = 30* °C.

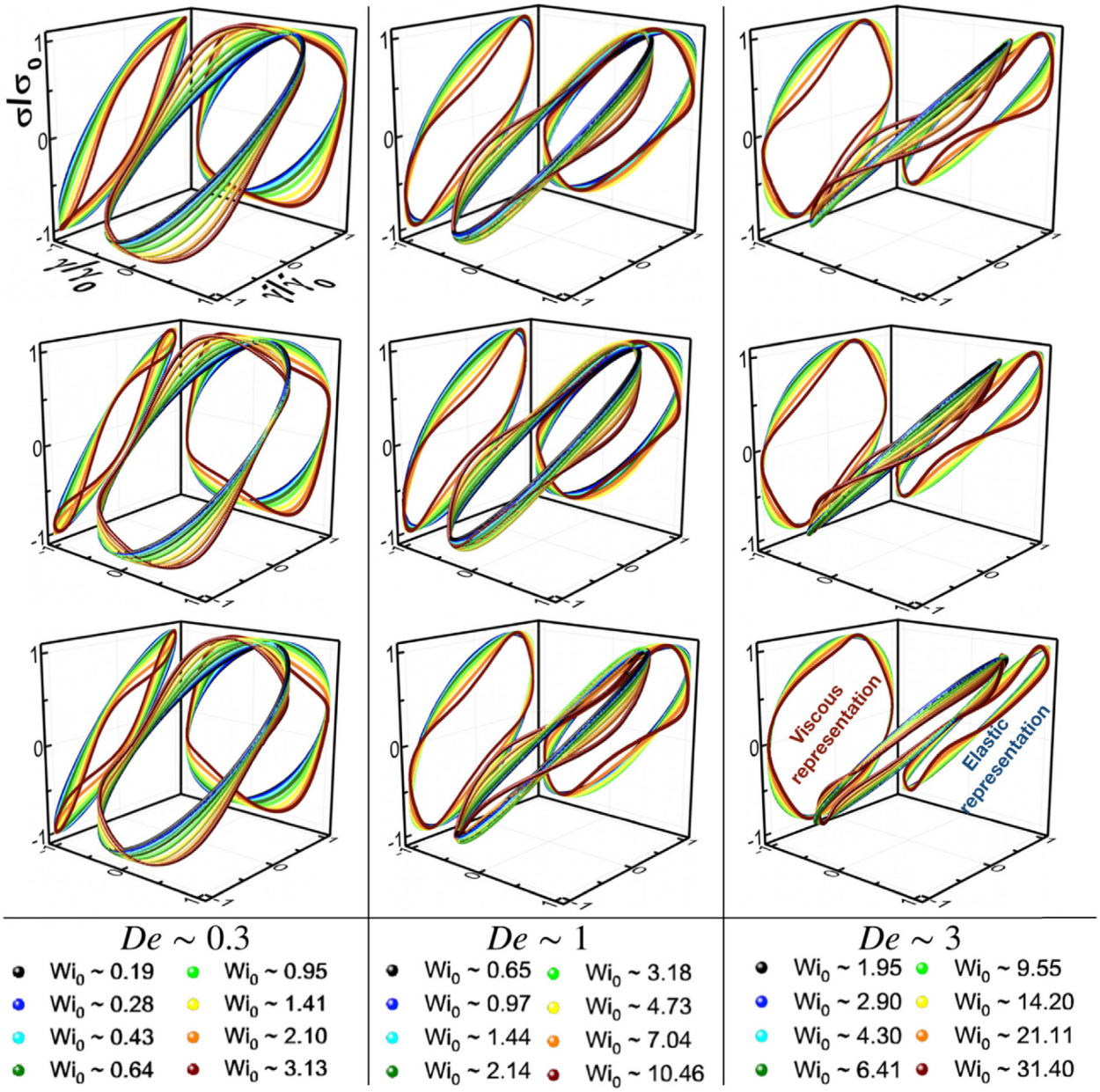

Fig. 5. Normalized 3D Lissajous-Bowditch curves and their projections (elastic representation: σ/σ_o *vs.* γ/γ_o or viscous representation: σ/σ_o *vs.* $\dot{\gamma}/(\gamma_o\ \omega)$) for CTAB/NaSal micellar solution for $R = 4$, at different Wi_o ($=\tau_R\omega\ \gamma_o$) and De ($=\tau_R\omega$). Temperature from the upper to the lower row $T = 20$, *25,* and *30* °C, respectively; *[CTAB] = 0.1 M.*

graphs, the amplitude of shearing strain, $\gamma_o = Wi_o/De$, varies, depending on the case, from a little less than 1, up to $\gamma_o \sim 10$ (curves with a different color). Fig. 4 presents for CTAB/$NaNO_3$ micellar solution, the 3D Lissajous-Bowditch curves, and their projections. As mentioned, this system presents shear banding in steady shear for the concentration above *0.1 M* in CTAB (systems in the two upper rows of Fig. 4). For $De \sim 0.3$, for $Wi_o/De \leq 1$, linear viscoelasticity is observed since the shape of the σ/σ_o *vs.* γ/γ_o curves are ellipsoidal in the elastic representation; their maximum stress is also in the first quadrant of this representation. On the contrary, as $Wi_o/De > 1$, the ellipsoidal shapes are lost, and the stress maxima move to the second quadrant in the elastic representation, *i. e.*, their behavior is nonlinear. For $De \sim 1$, the behavior is the same as for $Wi_o/De \leq 1$, the σ *vs.* γ curves describe ellipses; but when $Wi_o/De > 1$, the curves show a behavior more nonlinear than in the previous case, except for the case of the lower CTAB concentration (lower row, [CTAB] = *0.1*). Here, the system's behavior seems viscoelastic since the σ *vs.* γ curves describe elliptical shapes in the elastic representation. For $De \sim 3$, the behavior is viscoelastic for most solutions. Although for the case of the solution with the largest CTAB concentration, as the Wi_o/De increases over 1, the σ/σ_o *vs.* γ/γ_o curves in the elastic representation become less ellipsoidal, deviating from the Maxwell model to showing a more clear nonlinear behavior. For the lower CTAB concentration case ([CTAB] = *0.1*), the behavior of the σ *vs.* γ curves corresponds to a linear elastic response, as observed in the elastic (forming almost a diagonal line) and viscous representations (forming almost a circle). The elastic contribution makes the fluid behavior more nonlinear as more CTAB is added to the solution, which is also the direction of increase in τ_R.

From the mesoscopic point of view, as CTAB concentration increases, the total WLM contour length increases, as well as the degree of entanglement of the micellar network, as we will show below. This is one of the underlying reasons for the increase of

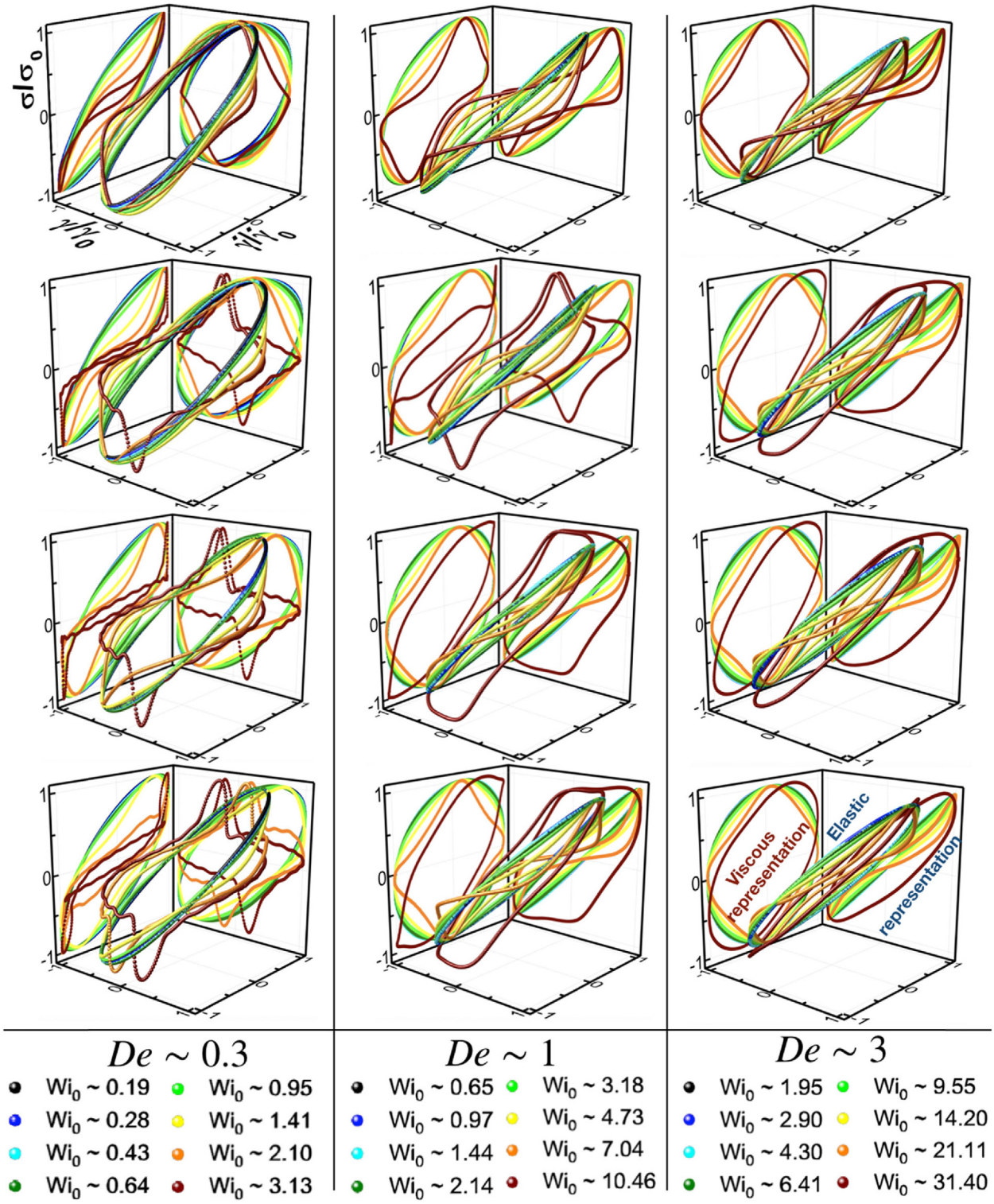

Fig. 6. Normalized 3D Lissajous-Bowditch curves and their projections (elastic representation: σ/σ_o *vs.* γ/γ_o or viscous representation: σ/σ_o *vs.* $\dot{\gamma}/(\gamma_o\ \omega)$) for CTAB/NaSal micellar solution for $R = 2$, at different Wi_o ($=\tau_R\omega\ \gamma_o$) and De ($=\tau_R\omega$). Temperature from the upper to the lower row $T = 20, 25, 30,$ and 35 °C, respectively; *[CTAB] = 0.1 M.*

an elastic contribution on the forces involved in the flow and the nonlinear response. The behavior described for the CTAB/$NaNO_3$ system is similar to that described by the Lissajous–Bowditch curves in LAOStrain given by the nRP model with a nonmonotonic constitutive curve given in Fig. 6 of Ref. [33] described in the introduction (note that in that study, the units make $\tau_R = 1$).

In Fig. 5, we present the 3D Lissajous-Bowditch curves and their projections for CTAB/NaSal for $R = 4$. In this WLM solution, shear banding in steady shear is never observed when the temperature is varied [24]. Although the Lissajous–Bowditch curves and their projections are not equal to the case of CTAB/$NaNO_3$, they are relatively similar. In all the cases with $Wi_o/De \leq 1$, the system follows a viscoelastic linear flow because the σ/σ_o *vs.* γ/γ_o curves describe

an ellipse, and the stress maxima are in the first quadrant in the elastic representation. However, when $Wi_o/De \geq 1$, WLM solutions do not follow the ellipsoidal shape revealing a nonlinear behavior. In $De \sim 3$, although the behavior is nonlinear, the elastic contribution seems to be more important than in $De \sim 0.3$, because, in the σ/σ_o *vs.* γ/γ_o representation, the curves present relatively more elongated diagonal shapes and relatively more circular shapes in the σ/σ_o *vs.*$\dot{\gamma}/(\gamma_o\ \omega)$) representation. This is particularly clear in the direction where τ_R decreases (higher temperatures) and entanglement decreases, as we will see below. In agreement with the LAOStrain results given by the nRP model with a monotonic constitutive curve [33], we expect that shear banding could appear during the experimental development of the Lissajous-Bowditch curves at some specific shear deformations.

In contrast with the cases presented in Figs. 4 and 5, Fig. 6 shows very different results for the CTAB/NaSal micellar solution for $R = 2$. This system presents gradient shear banding under steady flow, but as we reported before [24] and discussed below, the bands do not show a simple scenario; several bands are observed. In general, in all the cases of this micellar system with $Wi_o/De \leq 1$, a viscoelastic linear flow is observed because the σ/σ_o *vs.* γ/γ_o curves describe elliptical shapes, and the stress maxima are in the first quadrant in the elastic representation. For $Wi_o/De > 1$, different behavior is followed going to the right in a row. At $De \sim 0.3$, the response of WLM solutions to oscillatory shearing strain is nonlinear and going downward in the figure (higher temperatures and lower τ_R), there is a significant increase in the shear stress, which are stress overshoots. As far as the *De* number increases, these stress overshoots are not so prominent at particular τ_R; they almost disappear at $De \sim 3$.

At $De \sim 0.3$, the ratio of relaxation time to the time scale of deformation observation is relatively small, and we observe a quasi-steady response that must be in some way similar to what is observed in a steady flow, as described above. In the elastic or viscous representations, we observe significant oscillations. We suspect that the oscillations could be due to the formation of multiple bands when the system reaches that region of the cycle, as it occurs during steady shear flow, as shown in the next section. As far as $De \sim 1$ with $Wi_o/De > 1$, the nonlinear behavior is substantial, but there are no oscillations as in $De \sim 0.3$. However, at $De \sim 3$ with $Wi_o/De > 1$, the system behaves nonlinearly in the upper rows (lower temperatures and larger τ_R), but the system becomes relatively more viscoelastic in the lower ones. Here, τ_R is smaller, as well as entanglement. We will discuss this issue below.

It is important to note the following fact after depicting the 3D Lissajous-Bowditch curves and their projections for three different WLM solutions, which due to the temperature or surfactant concentration, present different τ_R values. Despite being scaled Pipkin diagrams, several systems for the same *De* and Wi_o numbers in a column do not reflect a scaled invariance; some curves corresponding to the same color are similar but quite different in other cases. We suspect that is due to the degree of entanglement of the micellar network, which is responsible for elastic forces and different for each WLM solution, but not considered in the description yet. The micellar network needs to be disengaged during the LAOS protocol. In particular, at high frequencies, as in the case of $De \sim 3$ with $Wi_o/De > 1$, systems with large τ_R cannot be disentangled efficiently; then, their degree of nonlinear behavior is relatively large. We will go back to this issue below.

3.3. Observation of the gradient shear bands

The external cylinder is rotating in our setup, and the internal one is fixed. It is well known that the inertial Taylor instability does not occur when the outer cylinder is rotating, as in our case. In contrast, instabilities do not depend on which cylinder is rotating in the purely elastic analog [44]. At low dimensionless curvature of the streamlines ($\Lambda = d/R_i$), shear banding does not show secondary flow instabilities [26]. In our case, $\Lambda = 0.066$. Therefore, we expected only to observe an instability because the WLM solutions become inhomogeneous close to $Wi \sim 1$ and $\sigma/G_0 \sim 1$. Along the flow curve plateau, where the fluid becomes inhomogeneous, scattered light coming off a page of light in the gap of a Couette cell geometry (gradient-vorticity plane) made of two transparent concentric quartz cylinders allows the observation of gradient shear bands because of nematic phases scatter light much more than an isotropic phase.

We developed thixotropic loops giving long or short deformation times to the fluid with respect to τ_R ($t^{rel} > 1$ or $t^{rel} < 1$). Typical images of what is observed in the gap in the gradient-vorticity plane can be seen in Fig. 7a for WLM solutions of CTAB/NaSal for $R = 2$ and 25 °C. In all cases, a paranematic phase appears close to the moving cylinder (external one) in the up-shear curve at $Wi \sim 1$. As the shear rate increases, more bands are formed. However, there is no simple scenario with just one paranematic band close to the moving cylinder. Although curves are relatively more stable for $t^{rel} > 1$, the paranematic phase is pretty dynamic, forming and reforming themselves in different positions along the gap, wriggling, and changing their shapes; After several experiments, there is no significant difference if t^{rel} is greater or lesser than one. The scattered intensity is constant on the average along the gap at a fixed shear rate; the average increases as the shear rate increases. As the *Wi* number increases, bands are thicker, and most of the time, there is not just one band. The contrast between isotropic fluid and the paranematic fluid (dark and brighter regions) seems higher after a long time. Although certainly, it is difficult to find clear trends or differences. The conclusion is that the position where bands are formed and their size are random. We consider that there is much room for theoretical developments about these instabilities.

Image processing provides spatiotemporal characteristics of the observed bands during the shear banding. In the central part of the gradient-vorticity plane, from video recordings of the bands, a light intensity distribution $I(x)$ from a horizontal line along the gradient direction was sampled at regular time intervals to produce space-temporal diagrams $I(x,t)$ of the flow pattern. These space–time plots are helpful for determining the onset and evolution of flow transitions and instabilities. Fig. 7b presents an example of a space–time plot for CTAB/NaSal WLM solutions for $R = 2$ and 25 °C, where some features are relatively straightforward. At $t^{rel} > 1$, the contrast between paranematic bands and isotropic fluid is lower, revealing fewer fluctuations and more stable bands, although it is not common to observe just one band. At $t^{rel} < 1$, there are also many bands, and light scattering is more intense in the paranematic and isotropic fluids. We suspect that the flow is less stable due to the fluctuation increase. Experiments with CTAB/NaSal for $R = 4$ do not show shear bands, and CTAB/$NaNO_3$ presents just one band close to the moving cylinder (simple scenario) under similar conditions as in our experiments, see Ref. [26].

3.4. Mesoscopic parameters

The main mesoscopic scales that characterize the micellar solutions' micellar network are L_C, l_p, l_e, and ξ. Fig. SM4 is an example of the results of our procedure, which is presented for a CTAB/$NaNO_3$ solution (original experimental data in Fig. SM2). The inset of Fig. SM4a presents the intensity correlation function of the scattered light coming from a WLM solution with embedded microspheres, and Fig SM4a presents the *MSD* of these particles calculated from the intensity correlation function. Fig SM4b presents the calculated viscoelastic spectra $G'(\omega)$ and $G''(\omega)$ derived

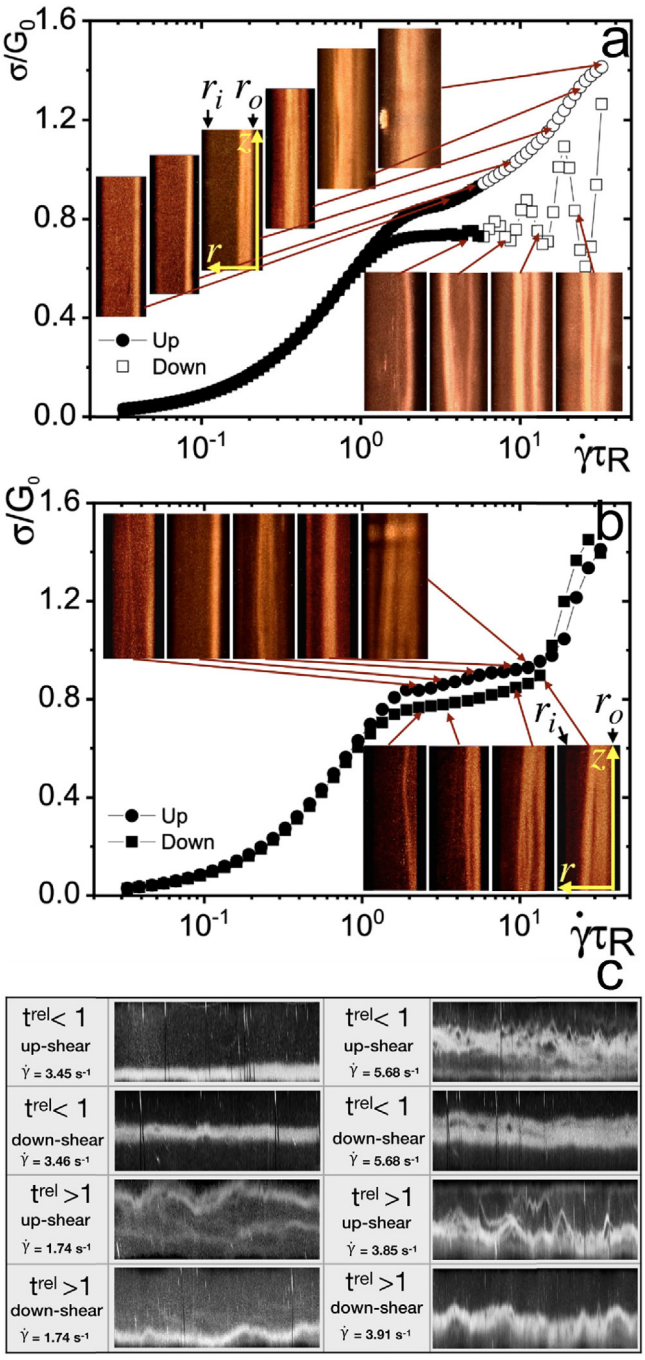

Fig. 7. Gradient shear banding in CTAB/NaSal WLM solutions for *R = 2* and *25 °C* as observed in the gap with a page of light in the gradient-vorticity plane (the color is artificial); r_i and r_o inner and outer radius of the gap, respectively. a) and b) Flow curves σ *vs.* for thixotropic loops. Up-shear curves (Up) are circles, and down-shear (Down) curves are squares. Full symbols correspond to measurements where $t^{rel} > 1$, and empty symbols correspond to $t^{rel} < 1$. The images are observations approximately where the arrows are pointing out. c) Space-time plot grayscale images: Horizontal light intensity on a line of pixels along the gradient direction (vertical) *vs.* time (horizontal) for CTAB/NaSal WLM solutions, for *R = 2* during thixotropic loops. Bright regions correspond to the paranematic fluid. They correspond to the images in (a) and (b) at some particular time. The external cylinder is rotating (bottom of the space–time graphs), and the inner cylinder is fixed (top of the space–time graphs).

from the best fit of the MSD data using the Bellour method [33-36], which goes from low to high frequencies, and the inset of Fig. SM4b presents the change of the power-law exponent of $|G^*|$ at high frequencies, from $\nu \sim 5/9$ to $\nu \sim 3/4$. Once G_o, G''_{min}, and ω_o are determined, the characteristic lengths can be evaluated [35-38]. The results for different surfactant concentrations and temperatures of the solutions on discussion here are in Table 1. These quantities change when the amount of surfactant, the ratio of salicylate to surfactant, temperature, or ionic strength of the media vary. Details about interpretation and analysis of the results have been done elsewhere [35-38].

3.5. Dimensionless elasticity number and mesoscopic entanglement index

In WLM solutions, the *Wi* number takes the role of a control parameter in steady shear flow, which compares elastic to viscous forces in the fluid, as shown in the scaled curves (σ/G_o *vs.* $\dot{\gamma}\tau_R$) shown above. When *Wi* < 1, the fluid's elastic to viscous forces ratio is small. Apparently, the micellar network is under a slowly disentangling viscous flow since the deformation rate is slow. When Wi $\sim$ 1, there is a regime change from linear to nonlinear, as displayed below a scaled critical temperature in a master dynamic phase diagram, where an isotropic and a paranematic phase coexist [45]. Here, the fluid shear thins, and the σ/G_o *vs.* $\dot{\gamma}\ \tau_R$ curve presents a stress plateau. As *Wi* grows up above 1, elastic forces in the fluid are more significant than the viscous forces since viscosity decreases as $\dot{\gamma}$ increases along the coexistence region. Fig. 8a presents *El* (=*Wi*/*Re*) *vs. Wi* for the micellar solutions studied here (details to make these curves in Fig. SM5). At *Wi < 1*, inertial forces are negligible compared to those related to elastic deformations suffered by the micellar network. Here, *El* is relatively constant and can reach several orders of magnitude depending on the system. When *Wi* $\sim$ *1*, *El* starts to decay linearly following the instantaneous viscosity as observed when *Wi > 1*, and *El* can decrease more than one order of magnitude in some systems (CTAB/NaSal), although their *El* values can be still pretty significant. We can also observe that the larger *El*, the lower temperature in the CTAB/NaSal systems, and in CTAB/$NaNO_3$, the larger the surfactant concentration, the larger *El*. That trend is similar to that followed by τ_R given for all systems in Fig. 1. The isotropic-paranematic transition is observed in CTAB/NaSal solutions with *R = 2* at very high *El* values. The CTAB/NaSal solutions with *R = 4* also have high *El* values; however, they are not as high as with *R = 2*, but do not present that phase transition. For the case of CTAB/$NaNO_3$, where *EI* values are orders of magnitudes below those of the CTAB/NaSal systems, shear banding transition is present just for the larger values of elasticity. Nevertheless, it does not appear for the lowest *El* value. More cases need to be studied to determine if there is a tendency to find shear banding when *El* grows.

The *Re* and *Wi* numbers are ratios between different forces involved in the fluid flow, which also depend on the flow conditions. However, they are not measuring directly any intrinsic property related to the elasticity of the micelle network that is perturbed when the fluid slowly flows. This is particularly obvious when *Wi < 1*, where inertial forces are negligible, due to the low speed of the fluid flow, with respect to those related to elastic deformations suffered by the micellar network, which is slowly disentangling during that deformation. Here, the mesoscopic scales *Lc* and l_e could be of help. We can evaluate the number of entanglements that an average micelle has close to equilibrium by measuring the mesoscopic scales of a micellar network as presented above. It would be pretty reasonable that as there are more entanglements per micelle, the micelle network could react more elastically to any slow deformation while trying to disentangle. Therefore, we define an entanglement index, $\kappa = L_c/l_e$, for WLM solutions. Our group has used this ratio to explain the viscosity dependence on temperature in some micellar solutions because entanglement decreases on increasing temperature, which also

Table 1
The mesoscopic scales that characterize the micellar solutions' micellar network.

	$\xi(nm)$	$l_p(nm)$	$l_e(nm)$	$L_C(nm)$	$\kappa = L_C/l_e$
[CTAB]	$NaNO_3$/CTAB, [$NaNO_3$] = 0.3 M, and 30 °C				
0.1 M	119.1	35.7	265.8	1974.4	7.4
0.2 M	89.7	27.9	195.6	1745.2	8.9
0.3 M	85.0	22.7	204.7	2159.3	10.5
T (°C)	NaSal/CTAB, [CTAB] = 0.1 M, and R = 4				
20	95.5	24.8	234.4	4611.2	19.7
25	100.4	21.4	281.3	3018.1	10.7
30	109.9	15.3	409.3	3845.4	9.4
T (°C)	NaSal/CTAB, [CTAB] = 0.1 M, and R = 2				
20	104.7	17.0	352.5	12416.3	35.2
25	102.5	20.1	303.8	8271.7	27.2
30	104.0	22.5	288.1	3921.6	13.6
35	102.3	36.2	204.6	1967.2	9.6

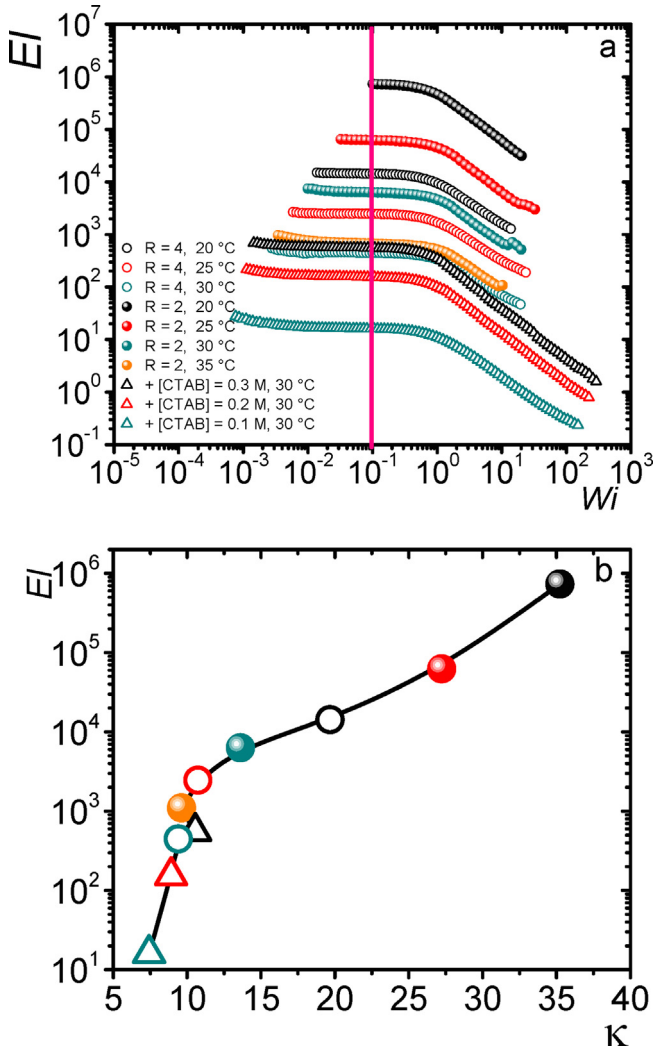

Fig. 8. a) *El* (=*Wi*/*Re*) *vs. Wi* (=$\dot{\gamma}\ \tau_R$) for the micellar solutions of CTAB/NaSal ([CTAB] = *0.1 M*), for *R = 2* and *R = 4*, at different temperatures, and of *CTAB/$NaNO_3$* ([*CTAB*] from *0.1* to *0.3 M*, and [*$NaNO_3$*] = *0.3 M*), at 30 °C. b) *El vs.* κ for the WLM solutions, where *El* is calculated along the vertical red line showed in (a), for a Couette cell with *d = 2.5 mm*, R_i = *37.5 mm*, Λ = *0.066*.

explains why the elasticity number measured in Couette flow decreases as the temperature increases [37,38]. Other authors have started using the parameter $Go\ /G''_{min}$, close to our definition, to measure entanglement [46]. In Fig. 8b, we observe that when κ increases, *El* also increases nonlinearly; a big shoulder appears at $\kappa \sim 10$, apparently separating two regimes. It is unclear if these regimes could be related to a contribution change between inertial and elastic forces to *El*. More theoretical development is needed to understand this feature. The large values in κ are the underlying reason for observing in some WLM solutions so large values of *El* at small values of *Wi*; this is the case of CTAB/NaSal solutions with a significant κ value, in contrast with those of CTAB/$NaNO_3$ where κ is much lower.

Flow curves are essentially the same in thixotropic loops when $t^{rel} > 1$, as discussed above, no matter what protocol or cylinder of the Couette geometry is rotating. Although the micellar network is under strain by the flow, there is enough time for a slowly disentangling. Nevertheless, when $t^{rel} < 1$, flow curves do not coincide and present large fluctuations because there is no time for the micellar network to be disentangled, so the response to the strain of the micelle network in the fluid is quite elastic and nonlinear. Thixotropic loops that present multiple bands correspond to micellar solutions with a significant degree of entanglement, κ, as is the case for CTAB/NaSal with *R = 2*. However, CTAB/NaSal with *R = 4* does not show shear bands, where κ is lower than for *R = 2*. In contrast, for CTAB/$NaNO_3$ solutions, κ is relatively low, and when they present banding, it is just one band close to the moving cylinder (simple scenario). It is unclear why CTAB/NaSal with *R = 4* does not present shear banding with such a high entanglement. We are probably extrapolating too much the concept of κ, which was measured in equilibrium, and another component related to the dynamics of the shear banding formation plays an important role.

As mentioned above, in the Lissajous-Bowditch curves, in a specific column, τ_R, is different going downwards. Pipkin diagrams in scaled variables for the same *De* and Wi_o numbers do not reflect scaled invariance. Just curves corresponding to the same color where $Wi_o < 1$ are almost superimposable. However, when $\gamma_o = Wi_o/De$ increases, the micellar network is highly deformed, which is harsher in LAOS at high frequencies because micelles do not have enough time to disentangle at the speed of the imposed strain. Then, the larger κ, the more nonlinear behavior will be expected. However, in LAOS experiments, we cannot evaluate κ along the deformation steps in the experiment in the present state of our knowledge because these experiments are developed far from equilibrium as ω increases. The index κ is obtained in equilibrium conditions. It cannot be used as *Wi* or Wi_o notoriously increase because the micellar network is disentangling, and micelles start to align due to the flow. In such a case, the equilibrium κ index no longer represents the entanglement. Developments for evaluating mesoscopic quantities in nonequilibrium conditions, experiments, or theory would be welcome to understand better how the rheological response is related to changes in mesoscopic scales in dynamic environments, like those observed during shear banding in LAOS cycles [29] or in shear thickening [48]. However, κ can give us a clue of what is happening in the system by extrapolating what is occurring at low values of *Wi*.

As mentioned above, we suspected that the degree of entanglement of the micellar network, which is responsible for elastic forces, must be substantial. This seems to be correct from the data in Table 1. For the CTAB/$NaNO_3$ solutions, as the CTAB concentration increases, the micellar length, L_C, does not vary so much, although it increases at the higher concentration. However, l_e slightly decreases as the CTAB concentration increases; therefore, the degree of entanglement, κ, increases. In the CTAB/NaSal solutions with $R = 4$, l_e decreases as temperature drops; L_C first decreases with temperature but increases at *25 °C*. Hence, the degree of entanglement given by κ increases as temperature decreases. Finally, in the case of CTAB/NaSal with $R = 2$ solutions, L_C notoriously increases when the temperature decreases and l_e also increases, but at a slow pace. Therefore, the entanglement notoriously increases. The micellar network can be slowly disengaged during the LAOS protocol at not-so-large γ_o and low frequencies, but not at high frequencies ($De \sim 3$ with $Wi_o/De > 1$). Finally, it is essential to mention three points: Micellar solutions with large κ cannot be efficiently disentangled; their degree of nonlinear elastic behavior is relatively large. Second, the physicochemical parameters of micellar solutions determine the mesoscopic scales; apparently, the other mentioned mesoscopic scales also change, but they do not have a clear impact on the rheological behavior as $\kappa = L_c/l_e$. Third, the exact disentanglement mechanism is unknown, and most likely several mechanisms are occurring at the same time: Micelles could slide or reptate to leave the entanglement through viscous flow, break and reform, or through the transient character of cross-links, where when a micellar thread collides or contact an entanglement, it forms a transient cross-link that recombines on the other side of the encountered topological constraint (ghostlike crossing).

4. Conclusions

In this study, we did different experiments (flow curves, small and large oscillatory shear tests, linear shear banding observations) to determine how elastic forces modify the rheological behavior of Maxwellian fluids due to the contribution of elastic forces to the flow. Also, we made diffusive wave spectroscopy micro-rheology to obtain the mesoscopic length scales of the entangled micellar network in WLM solutions, which are determined by the solutions' physicochemical parameters (concentration of surfactants, hydrotropic salts, temperature, the ionic force of the media, etc.). Our approach to understanding the origin of how the elastic forces affect the rheological behavior of micellar fluids is not through proposing a model and solving it for different experimental protocols, as mainly made for LAOS experiments in Refs. [31] and [32]. Our approach was to find a property that somehow measures entangling in the mesoscopic micellar network, giving rise to elastic forces opposing to the fluid deformation during flow. This property is the entanglement index, κ, which allows us to understand the consequences of the entanglement in the experiments we performed, explaining why different micellar systems are ordered in the way shown in the diagram *El vs. Wi* of Fig. 8a in terms of the characteristic length scales of the supramolecular structures, which self-assembles in the fluid. Mesoscopic simulation methods for predicting the rheology of WLMs [31,47] need to be done in the future to confirm the correlation between *EI* and κ, as observed in Fig. 8b, and to determine if the apparent two regimes observed in that figure have some physical insight.

Declaration of Competing Interest

The authors declare that they have no known competing financial interests or personal relationships that could have appeared to influence the work reported in this paper.

Acknowledgments

Financial support from SEP – CONACyT (A1-S-15587) and DGAPAUNAM (IN 106218) is gratefully acknowledged, and the CONACYT scholarship for R. F. L-S. We thank C. Garza and S. Ramos for their technical support.

Appendix A. Supplementary material

Supplementary data to this article can be found online at https://doi.org/10.1016/j.jcis.2022.07.003.

References

[1] R. Boyd, G. Smith (Eds.), Polymer Dynamics and Relaxation, Cambridge University Press, 2007.
[2] S. R. Raghavan;, Y. Feng, Wormlike Micelles: Solutions, Gels, or Both? In: C. A. Dreiss, Y. Feng (Eds). Wormlike Micelles Advances in Systems, Characterisation and Applications. Royal Society of Chemistry. (2017).
[3] A. Tavera-Vazquez, B. Arenas-Gomez, C. Garza, Y. Liu, R. Castillo, Soft Matter 14 (2018) 7264, https://doi.org/10.1039/c8sm01530a.
[4] M. Cates, Macromol. 20 (1987) 2289, https://doi.org/10.1021/ma00175a038.
[5] J.K.G. Dhont, W.J. Briels, Rheol Acta. 47 (2008) 257, https://doi.org/10.1007/s00397-007-0245-0.
[6] S. Manneville, Rheol Acta 47 (2008) 301, https://doi.org/10.1007/s00397-007-0246-z.
[7] S.M. Fielding, P.D. Olmsted, Eur. Phys. J. E. 11 (2003) 65, https://doi.org/10.1140/epje/i2002-10128-7.
[8] P.D. Olmsted, C.Y.D. Lu, Phys. Rev. E 60 (1999) 4397, https://doi.org/10.1103/PhysRevE.60.4397.
[9] S. Lerouge, J.P. Decruppe, J.F. Berret, Langmuir 16 (2000) 6464, https://doi.org/10.1021/la000269w.
[10] G. Porte, J.-F. Berret, J.L. Harden, J. Phys. II (France) 7 (1997) 459, https://doi.org/10.1051/jp2:1997138.
[11] M.E. Helgeson, M.D. Reichert, Y.T. Hu, N.J. Wagner, Soft Matter. 5 (2009) 3858, https://doi.org/10.1039/B900948E.
[12] B. Arenas-Gómez, C. Garza, Y. Liu, R. Castillo, J. Col. Interface. Sci. 560 (2020) 618, https://doi.org/10.1016/j.jcis.2019.10.052.
[13] S. Lerouge, M. Argentina, J.P. Decruppe, Phys. Rev. Lett. 96 (2006) 88301, https://doi.org/10.1103/PhysRevLett.96.088301.
[14] H.J. Wilson, S.M. Fielding, J. Non-Newtonian Fluid Mech. 138 (2006) 181, https://doi.org/10.1016/j.jnnfm.2006.05.010.
[15] S.M. Fielding, Phys. Rev. Lett. 95 (2005), https://doi.org/10.1103/PhysRevLett.95.134501 134501.
[16] S. Gravsholt, J. Col. Interface Sci. 57 (1976) 575, https://doi.org/10.1016/0021-9797(76)90236-8.
[17] C. Manohar, U.R.K. Rao, B.S. Valaulikar, R.M. Iyer, J. Chem. Soc., Chem. Commun. 379 (1986), https://doi.org/10.1039/C39860000379.
[18] T. Shikata, H. Hirata, T. Kotaka, Langmuir. 3 (1987) 1081, https://doi.org/10.1021/la00078a035.
[19] T. Holz, P. Fischer, H. Rehage, J. Non-Newtonian Fluid Mech. 88 (133) (1999), https://doi.org/10.1016/S0377-0257(99)00016-6.
[20] I.M. Alkschbirs, A.M. Perceboma, W. Loha, H. Westfahl, M.B. Cardoso, E. Sabadini, Coll. Surf. 470 (2015) 1, https://doi.org/10.1016/j.colsurfa.2015.01.052.
[21] E. Cappelaerre, J.-F. Berret, J.P. Decruppe, R. Cressely, P. Lindner, Phys. Rev. E. 56 (1997) 1869, https://doi.org/10.1103/PhysRevE.56.1869.
[22] J.P. Decruppe, O. Greffier, S. Manneville, S. Lerouge, Phys Rev. E. 73 (2006) 61509, https://doi.org/10.1103/PhysRevE.73.061509.
[23] S. Lerouge, J.P. Decruppe, C. Humbert, Phys. Rev. Lett. 81 (1998) 5457, https://doi.org/10.1103/PhysRevLett.81.5457.
[24] J. Delgado, H. Kriegs, R. Castillo, J. Phy. Chem. B. 113 (2009) 15485, https://doi.org/10.1021/jp9027996.
[25] C. Perge, M.A. Fardin, S. Manneville, Soft Matter. 10 (2014) 1450, https://doi.org/10.1039/c3sm52868e.
[26] M.A. Fardin, T.J. Ober, V. Grenard, T. Divoux, S. Manneville, G.H. McKinley, S. Lerouge, Soft Matter 8 (2012) 10072, https://doi.org/10.1039/c2sm26313k.
[27] K. Hyuna, M. Wilhelmb, C.O. Kleinb, K.S. Choc, J.G. Namd, K.H. Ahnd, S.J. Leed, R.H. Ewoldte, G.H. McKinley, Prog. Poly. Sci. 36 (2011) 1697, https://doi.org/10.1016/j.progpolymsci.2011.02.002.
[28] M.A. Calabrese, S.A. Rogers, L. Porcar, N.J. Wagner, J. Rheol. 60 (2016) 1001, https://doi.org/10.1122/1.4961035.
[29] S. Rogers, J. Kohlbrecher, M.P. Lettinga, Soft Matter 8 (2012) 7831, https://doi.org/10.1039/c2sm25569c.
[30] R.G. Larson, J. Rheol. 28 (1984) 545, https://doi.org/10.1122/1.549761.
[31] W. Zou, R.G. Larson, J. Rheol. 58 (2014) 681, https://doi.org/10.1122/1.4868875.
[32] R.L. Moorcroft, S.M. Fielding, Phys. Rev. Let. 110 (2013), https://doi.org/10.1103/PhysRevLett.110.086001 086001.
[33] K.A. Carter, J.M. Girkin, S.M. Fielding, J. Rheol. 60 (2016) 883, https://doi.org/10.1122/1.4960512.

[34] M.A. Fardin, C. Perge, N. Taberlet, Soft Matter. 10 (2014) 3523, https://doi.org/10.1039/C3SM52828F.
[35] J. Galvan-Miyoshi, J. Delgado, R. Castillo, Eur. Phys. J. E 26 (2008) 369, https://doi.org/10.1140/epje/i2007-10335-8.
[36] E. Sarmiento-Gomez, D. Lopez-Diaz, R. Castillo, J. Phys. Chem. B 114 (2010) 12193, https://doi.org/10.1021/jp104996h.
[37] N. Rincon-Londo, C. Garza, N. Esturau-Escofet, A. Kozina, R. Castillo, Col. Surf. 610 (2021), https://doi.org/10.1016/j.colsurfa.2020.125903 125903.
[38] A. Tavera-Vázquez, N. Rincon-Londoño, R.F. Lopez-Santiago, R. Castillo, J. Phys.: Condens. Matter 34 (2022), https://doi.org/10.1088/1361-648X/ac2c3e 034003.
[39] J. Delgado, R. Castillo, J. Col. Interface Sci. 312 (2007) 481, https://doi.org/10.1016/j.jcis.2007.03.010.
[40] T.G. Mason, Rheol. Acta 39 (2000) 371, https://doi.org/10.1007/s003970000094.
[41] N. Willenbacher, C. Oelschlaeger, M. Schopferer, P. Fischer, F. Cardinaux, F. Scheffold, Phys. Rev. Lett. 99 (2007), https://doi.org/10.1103/PhysRevLett.99.068302 068302.
[42] R. Granek, M.E. Cates, J. Chem. Phys. 96 (1992) 47589, https://doi.org/10.1063/1.462787.
[43] R. Granek, Langmuir. 10 (1994) 1627, https://doi.org/10.1021/la00017a051.
[44] R.G. Larson, E.S.J. Shaqfeh, S.J. Muller, J. Fluid Mech. 218 (1990) 573, https://doi.org/10.1017/S0022112090001124.
[45] J.F. Berret, G. Porte, J.P. Decruppe, Phys. Rev. E. 55 (1997) 1668, https://doi.org/10.1103/PhysRevE.55.1668.
[46] P. Rassolov, H. Mohammadigoushki, J. Rheol. 64 (2020) 1161, https://doi.org/10.1122/8.0000010.
[47] G. Tan, R.G. Larson, Rheol. Acta. 61 (2022) 443, https://doi.org/10.1007/s00397-022-01341-4.
[48] M. Takeda, T. Kusano, T. Matsunaga, H. Endo, M. Shibayama, T. Shikata, Langmuir 27 (2011) 1731, https://doi.org/10.1021/la104647u.